Proceedings of the 42nd Chinese Control Conference
July 24-26, 2023, Tianjin, China

Online Extrinsic Calibration of RGB and ToF Cameras for Extraterrestrial Exploration

Qinxuan Sun[1], Hang Shi[1], Yuehua Li[1], Qi Zhu[1], Zujie Ren[1]
1. Beijing Research Institute, Zhejiang Lab, Beijing 100086, P. R. China
E-mail: sunqinxuan@zhejianglab.com

Abstract: Extraterrestrial exploration is one of the most significant missions for the development of countries. Different sensors are used in an extraterrestrial exploration mission for different kinds of tasks, such as navigation and grasping. Correct extrinsic parameters for multiple sensors is fundamental for the performance of high-level tasks. Although the extrinsics can be accurately calibrated offline, they easily become inaccurate due to the vibration of the vehicle during the tasks. In this paper, an online extrinsic calibration algorithm is proposed for extraterrestrial exploration. Extrinsic parameters of RGB and ToF (time-of-flight) cameras are automatically adjusted while navigating the environment. The online calibration is achieved by the alignment of edges extracted from the RGB image and ToF intensity image, respectively. An edge registration algorithm is proposed and the probabilistic properties of pixels on edges are exploited for the alignment of the edges extracted from heterogeneous sensors. Experiments executed in the simulated extraterrestrial environment demonstrate effectiveness and efficiency of the proposed algorithm.

Key Words: Online calibration, Edge registration, Extraterrestrial exploration

1 Introduction

Navigating an extraterrestrial scene is a very challenging task due to the uncertainty in environments and limitations in communications (see Fig. 1). An exploration rover is usually equipped with multiple sensors for the perception and navigation of the extraterrestrial environments [1–3]. Among them, the visual sensor is one of the most important types of sensors [4–7]. RGB cameras can easily provide sufficient texture information for perception tasks. However, it is difficult for RGB cameras to reconstruct the structure of the environment. ToF cameras, on the other hand, have the advantages of dense range measurements and also the fast scanning speed [8, 9]. But the resolution of ToF cameras is often much lower can RGB cameras. As a result, it is significantly beneficial to combine them together for a better performance of the whole system [10–13].

To obtain an efficient fusion of the perceptual information from RGB and ToF cameras, an accurate calibration result is required. There have been some related works on the calibration of RGB and ToF cameras. Zhu et al. [14] introduced an empirical calibration method, which builds a look-up table mapping observed intensity and 3D positions to ground-truth distance. Gao et al. [15] proposed a joint extrinsic calibration method for a ToF-IMU-RGB-camera system. Specifically, a pattern was designed with white circles on a black background and the measurement errors were corrected using an error distribution model with a B-spline function. Jung et al. [16] presented a calibration method of a ToF and color camera pair by designing a 2.5D pattern board with irregularly distributed holes on it. And the ray correction and range bias correction are performed to improve the accuracy of the 3D measurements of a ToF camera.

(a)

(b)

Fig. 1: The extraterrestrial scenes on (a) Lunar and (b) Martian surfaces.

However, for all the above mentioned methods, an off-line calibration procedure is performed. As can be seen in Fig. 1, rugged terrains are contained in the extraterrestrial environments, and the extrinsic parameters can easily become inaccurate because it is impossible for the rover to move smoothly. As a result, it

This work was supported by the National Key R&D Program of China (2022YFB3903800), and National Natural Science Foundation of China under Grant U21B6001.

is important to automatically adjust the extrinsic parameters during the exploration process. Huang et al. [17] proposed a simple and efficient calibration method for a system composed by a Kinect V2 and color cameras, using point correspondences between the depth and color images. Nevertheless, for the challenging terrains in extraterrestrial environments, it is impossible to efficiently extract and match visual point features between the ToF and RGB camera pair [18].

Compared with visual point features, edges can be robustly extracted and matched from heterogeneous visual cameras [19]. Edges are extensively utilized in the online calibration of camera and LiDAR [20–22]. For the extraterrestrial environments, there are hardly any efficient edges extracted from the depth image because of the terrain. However, the intensity image captured by a ToF camera can be used for edge extraction, because the intensity measurements are related to the material of the object surfaces.

In this paper, we proposed an online extrinsic calibration algorithm for RGB and ToF cameras. The extrinsics of RGB and ToF cameras are adjusted online while exploring the extraterrestrial environment. Edges are extracted from the RGB image and ToF intensity image, respectively. Then, the edges are aligned in the RGB image through an ICP (iterative closest point)[23]-style registration process. The cost function of the optimization is specifically designed for the 2D edge registration.

2 Edge Registration-based Online Calibration

In this section, an ICP-based edge registration algorithm is proposed for the online calculation of the extrinsic parameters between the ToF and RGB cameras. First of all, the canny edges are detected in both the intensity image captured by a ToF camera and the RGB image captured by a visual camera. Then, the camera projection model is introduced for the projection of a pixel on the ToF intensity image onto the corresponding pixel on the RGB image plane. Next, the ICP-based edge registration algorithm is presented, exploiting the probabilistic characters of pixels on edges. Finally, the extrinsic parameters between the two cameras are optimized via the edge registration process. In the following, the online calibration algorithm is presented in detail.

Table 1: Selection of high and low threshold values for Canny edge detection.

Canny thresholds	high threshold	low threshold
RGB image	200	150
ToF intensity image	20	10

2.1 Canny Edge Detection

The Canny edge detection is used in our method, which is a popular edge detection algorithm developed by John F. Canny in [24]. In the experiment, we use the Canny edge detection implemented in OpenCV library.

The Canny edges are extracted from the RGB image and ToF intensity image, respectively. Note that the resolution of the RGB image (2048×2048) is much higher than that of the intensity image (640×480). Therefore, it needs to be careful in selecting the high and low threshold values for Canny edge detection [24]. In our implementation, we test different combinations of threshold values for the two kinds of images. It turns out that the threshold values listed in Tables 1 yield the best performance of the system.

2.2 Camera Projection Model

The pixel coordinates in ToF intensity image can be projected onto the RGB image plane, given the intrinsic parameters of the two cameras as well as the extrinsic parameters between them. Because the depth information is obtained for each pixel of the ToF intensity image and the 3D point in the ToF camera coordinate system can be reconstructed.

For a pixel $\boldsymbol{u}_t$ in the intensity image, the corresponding depth measurement is denoted by $\mathcal{D}(\boldsymbol{u}_t)$. The 3D point $\boldsymbol{p}_t$ in the ToF camera coordinate system corresponding to $\boldsymbol{u}_t$ can be computed by

$$\boldsymbol{p}_t = \pi^{-1}\left(\boldsymbol{u}_t, \boldsymbol{K}_t, \mathcal{D}(\boldsymbol{u}_t)\right) \tag{1}$$

where $\boldsymbol{K}_t$ is the intrinsics of the ToF camera, which is calibrated offline. The function $\pi^{-1}(\cdot)$ is the inverse projection of the ToF camera model, which can be uniquely solved given the depth measurement $\mathcal{D}(\boldsymbol{u}_t)$ for the pixel.

If the extrinsics between the ToF and RGB cameras are known, the 3D point $\boldsymbol{p}_c$ in the RGB camera coordinate system is calculated by

$$\boldsymbol{p}_c = \boldsymbol{R}_{ct}\boldsymbol{p}_t + \boldsymbol{t}_{ct} \tag{2}$$

where $\boldsymbol{R}_{ct} \in \mathbb{SO}(3)$ and $\boldsymbol{t}_{ct} \in \mathbb{R}^3$ represent the extrinsics between the two cameras, i.e., the rotation and translation, respectively, from the ToF coordinate system to the RGB camera coordinate system. Then, the pixel coordinates on the RGB image plane can be computed by

$$\boldsymbol{u}_c = \pi\left(\boldsymbol{p}_c, \boldsymbol{K}_c\right) \tag{3}$$

where $\boldsymbol{K}_c$ is the intrinsics of the RGB camera obtained from an offline calibration process.

2.3 ICP-based Edge Registration

Based on the camera projection model introduced in the previous sub-section, an ICP-based edge registration algorithm is presented for an online calibration of the two sensors. Specifically, an overall cost function is designed to align the edges extracted from the RGB and ToF intensity images, respectively. In each iteration of the ICP process, the correspondences are established using the previous estimate of the extrinsic parameters. Then, the optimization is performed to minimize the cost function based on the newly established correspondences. Different from the ICP algorithm for the 3D point cloud registration, we use the residuals between edges from two images to constrain the transformation

between the two sensors. And the local probabilistic properties of the pixels on edges are modeled and utilized in the optimization process.

The pixels on Canny edges extracted from the RGB and ToF intensity images are denoted by $\{\boldsymbol{u}_{c,i}, i = 1, \cdots, N_c\}$ and $\{\boldsymbol{u}_{t,i}, i = 1, \cdots, N_c\}$, respectively. Note that the pixel coordinates with the same subscript i represent a correspondence obtained in each iteration. And N_c represents the number of the corresponding pairs of the pixels from two sensors. For each pixel on the edges, the covariance is estimated using the local distribution of pixels on the edges. Without loss of generality, we consider a pixel $\boldsymbol{u}_{c,i}$ on the RGB image. The calculation for the pixels on the ToF image is likewise.

First of all, a kd-tree structure is constructed using all the pixels on the edges. And the N nearest neighbors of $\boldsymbol{u}_{c,i}$ are searched using the kd-tree structure. In our experiment, we found that $N = 20$ yields the best performance in terms of accuracy and efficiency. Then, the covariance matrix corresponding to $\boldsymbol{u}_{c,i}$ is calculated by

$$\begin{aligned} \boldsymbol{\mu}_{c,i} &= \frac{1}{N}\sum_{j=1}^{N} \boldsymbol{u}_{c,i}^{j} \\ \boldsymbol{C}_{c,i} &= \frac{1}{N-1}\sum_{j=1}^{N}\left(\boldsymbol{u}_{c,i}^{j} - \boldsymbol{\mu}_{c,i}\right)\left(\boldsymbol{u}_{c,i}^{j} - \boldsymbol{\mu}_{c,i}\right)^{T} \end{aligned} \tag{4}$$

where $\boldsymbol{u}_{c,i}^{j}$ denotes the j-th neighbor of the pixel $\boldsymbol{u}_{c,i}$, $\boldsymbol{\mu}_{c,i}$ is the mean value of the N neighbors, and $\boldsymbol{C}_{c,i}$ represents the estimate of the covariance. To clarify the local probabilistic properties of the $\boldsymbol{u}_{c,i}$, perform the eigenvalue decomposition of $\boldsymbol{C}_{c,i}$, yielding the eigenvalues λ_1 and λ_2. Note that for a pixel on the edges, it is obvious that the eigenvalues satisfy $\lambda_1 \gg \lambda_2$. This property is utilized in the ICP-based edge registration presented in the following.

The cost function for the edge registration is defined as

$$E(\boldsymbol{T}_{ct}) = \sum_{i=1}^{N_c} \boldsymbol{r}_i^{T} \boldsymbol{C}_i \boldsymbol{r}_i \tag{5}$$

where

$$\boldsymbol{T}_{ct} = \begin{bmatrix} \boldsymbol{R}_{ct} & \boldsymbol{t}_{ct} \\ \boldsymbol{0}^{T} & 1 \end{bmatrix} \in \mathbb{SE}(3) \tag{6}$$

and

$$\begin{aligned} \boldsymbol{r}_i &= \boldsymbol{u}_{c,i} - \pi\left(\boldsymbol{R}_{ct}\left(\pi^{-1}(\boldsymbol{u}_{t,i}, \boldsymbol{K}_t, \mathcal{D}(\boldsymbol{u}_{t,i}))\right) + \boldsymbol{t}_{ct}, \boldsymbol{K}_c\right) \\ \boldsymbol{C}_i &= \boldsymbol{C}_{c,i} + \boldsymbol{R}_{ct}\boldsymbol{C}_{t,i}\boldsymbol{R}_{ct}^{T} \end{aligned} \tag{7}$$

In our method, the cost function (5) is specifically designed for the 2D edge registration, as is illustrated below. In the conventional ICP process, the edge pixels are associated via a nearest-neighbor search procedure. As a result, the corresponding pixels may not be located on the similar structure. As shown in Fig. 2(a), the pixel $\boldsymbol{u}_{t,i}$ is associated to $\boldsymbol{u}_{c,j}$ according to the nearest-neighbor criterion. However, it is obvious that according to the geometrical structure, $\boldsymbol{u}_{t,i}$ and $\boldsymbol{u}_{c,j}$ are not the corresponding pixels. In our algorithm, the contribution of the residual of the wrong correspondences $\boldsymbol{u}_{t,i}$ and $\boldsymbol{u}_{c,j}$ is decreased by exploiting the local probabilistic properties of the pixels on edges. Specifically, for the covariance of $\boldsymbol{u}_{t,i}$, the eigenvalue λ_1 along the direction of the local edge is much greater than the eigenvalue λ_2 along the normal direction of the edge, as can be seen in Fig. 2(b). That is to say, each pixel on the edge provides a strong constraint along the normal direction, which aligns the edges strongly to each other along the normal.

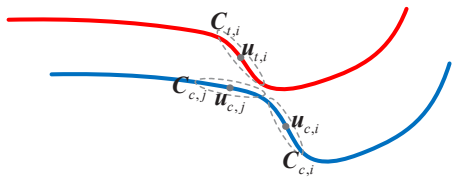

(a)

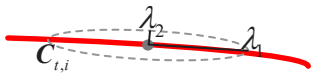

(b)

Fig. 2: Intuitive illustration of the local probabilistic property of edges.

2.4 Extrinsic Transform Optimization

In each iteration of the ICP-based edge alignment, the cost function (5) is optimized using Gauss-Newton algorithm. The extrinsic transform between RGB and ToF cameras is represented by $\boldsymbol{T}_{cr}$, as in (6). During Gauss-Newton optimization, the minimal representation is given by 6-dimensional vector $\boldsymbol{\xi} \in \mathbb{R}^6$, of which the corresponding element of the Lie algebra is given by

$$\boldsymbol{\xi}^{\wedge} = \begin{bmatrix} \boldsymbol{\rho} \\ \boldsymbol{\phi} \end{bmatrix}^{\wedge} = \begin{bmatrix} \boldsymbol{\phi}^{\wedge} & \boldsymbol{\rho} \\ \boldsymbol{0}^{T} & 0 \end{bmatrix} \in \mathfrak{se}(3) \tag{8}$$

where $\boldsymbol{\phi}^{\wedge}$ is the skew-symmetric matrix corresponding to the vector $\boldsymbol{\phi}$.

Rewriting the cost function (5) in a matrix style yields

$$E(\boldsymbol{T}_{ct}) = \boldsymbol{r}^{T}\boldsymbol{C}\boldsymbol{r} \tag{9}$$

where

$$\begin{aligned} \boldsymbol{r} &= \begin{bmatrix} \boldsymbol{r}_1^{T} & \boldsymbol{r}_2^{T} & \cdots & \boldsymbol{r}_{N_c}^{T} \end{bmatrix}^{T} \\ \boldsymbol{C} &= \begin{bmatrix} \boldsymbol{C}_1 & & & \\ & \boldsymbol{C}_2 & & \\ & & \ddots & \\ & & & \boldsymbol{C}_{N_c} \end{bmatrix} \end{aligned} \tag{10}$$

In the n-th iteration of the Gauss-Newton optimization algorithm, an increment $\delta\boldsymbol{\xi}^{(n)}$ is computed by solving a

second-order approximation of (9).

$$\delta\boldsymbol{\xi}^{(n)} = -(\boldsymbol{J}^T\boldsymbol{C}\boldsymbol{J})^{-1}\boldsymbol{J}^T\boldsymbol{C}\boldsymbol{r} \tag{11}$$

where $\boldsymbol{J}$ is the Jacobian matrix of the residual vector $\boldsymbol{r}$ with respect to the state vector.

$$\boldsymbol{J} = \frac{\partial \boldsymbol{r}}{\partial \boldsymbol{\xi}}\bigg|_{\boldsymbol{\xi}=\boldsymbol{\xi}^{(n)}} \tag{12}$$

After the incremental update $\delta\boldsymbol{\xi}^{(n)}$ is obtained, the extrinsic transform is optimized by

$$\boldsymbol{T}_{cr}^{(n+1)} = \exp(\delta\boldsymbol{\xi}^{(n)})\boldsymbol{T}_{cr}^{(n)} \tag{13}$$

where $\exp(\cdot)$ is the exponential map for matrix, which maps the element in the Lie algebra $\mathfrak{se}(3)$ to its correspondence in the Lie group $\mathbb{SE}(3)$.

3 Experiments

The proposed algorithm is tested in the simulated extraterrestrial environment, as shown in Fig. 3. The simulated scene is mainly composed of sand and stones, similar to the actual extraterrestrial environment. It can be obviously seen from Fig. 3 that the extraterrestrial environment is quite challenging for the commonly-used feature matching algorithm, like SURF and ORB features, etc. The experimental datasets are collected by an exploration rover equipped with a Blaze-101 ToF camera and a Mako G-419 RGB camera. The test platform is with an Intel Core i9-12950HX CPU at 2.30 GHz and 32GB RAM.

3.1 Experiments on Accuracy

The rover system is first calibrated offline with a pattern board. Then, the rover navigates and performs some certain tasks for a period of time. After that, four image sequences are collected in the simulated extraterrestrial scene that is shown in Fig. 3. The proposed edge registration-based online calibration algorithm is executed on every frame of the four sequences. Due to the highly challenging extraterrestrial environment, none of the current online calibration algorithms can be executed successfully. As illustrated in Fig. 4, the calibration outcomes are compared with the offline calibration based on the pattern board. The average re-projection errors for each sequence are listed in Tables 2. It can be seen that the re-projection errors of the proposed algorithm is much less than those of the traditional calibration procedure. Because the offline calibration results cannot be automatically adjusted during the navigation missions, they can easily become inaccurate, especially when the rover is running on the rugged terrain.

Different from the pattern board-based calibration method, the proposed online calibration based on the edge registration automatically adjust the extrinsics between ToF and RGB sensors. The extrinsic parameters are calculated in real-time using the measurement information by minimizing the re-projection errors. Therefore, even if the configuration of the sensors changes due to the vibration of the rover, the extrinsic parameters can be adjusted in time. For the navigation and manipulation missions, it is of great importance to maintain the accurate extrinsics of the sensors equipped on the rover. Because only if the calibration results between different sensors are kept accurate and stable, it is possible for the system to give good performance on the tasks which rely on the fusion of different onboard sensors.

(a)

(b)

Fig. 3: The simulated extraterrestrial environment.

Table 2: Average re-projection error over all the frames for the four sequences captured in the simulated environment.

Sequence	pattern board	edge registration
Sequence 1	4.78px	1.85px
Sequence 2	4.88px	1.82px
Sequence 3	4.96px	1.98px
Sequence 4	4.83px	1.54px

3.2 Experiments on Runtime

The real-time performance of the calibration algorithm is evaluated on the collected sequences. The runtimes on all the frames are computed and presented by the box-plot in Fig. 5. The median and mean values of the runtimes for each sequence are labeled by red solid line and blue dotted line, respectively.

In the experiments, we execute the calibration on

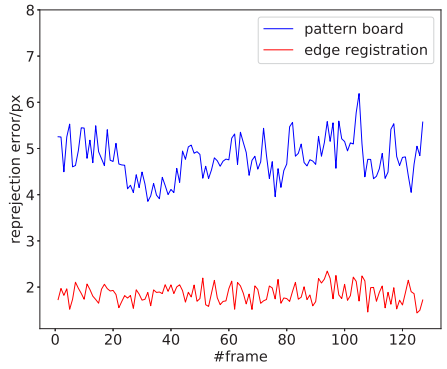

(a) Sequence 1.

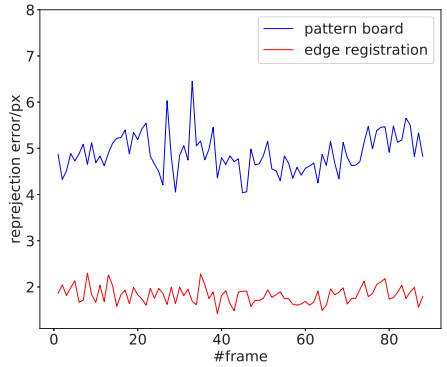

(b) Sequence 2.

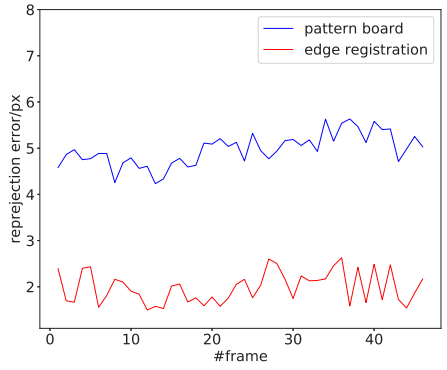

(c) Sequence 3.

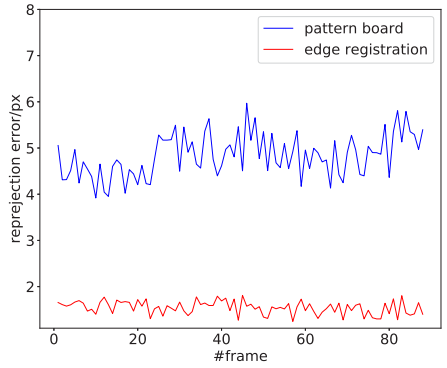

(d) Sequence 4.

Fig. 4: Comparison of the re-projection errors for four sequences captured in the simulated environment.

each frame of all the sequences to test the performance of the algorithm. Nevertheless, in the application, the online calibration only needs to be run at most once every several seconds to correct the extrinsic parameters, which may be slightly changed in a short period of time due to vibration. As can be seen from Fig. 5, the runtime of the online calibration procedure of our proposed algorithm is less than one second in most circumstances. As a result, the real-time performance of our algorithm can definitely support the online calibration during the exploration missions.

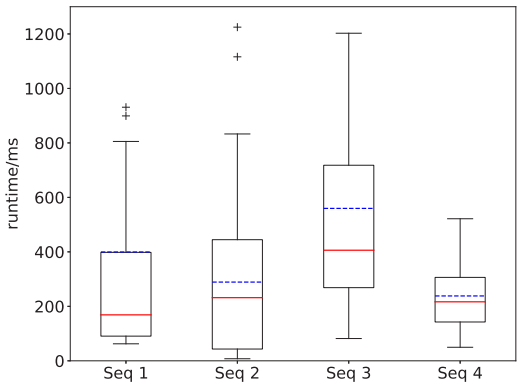

Fig. 5: Runtimes for four sequences captured in the simulated environment.

4 Conclusion

Because of the extremely challenging condition in the extraterrestrial environment, existing online calibration method cannot be utilized directly for the extraterrestrial exploration tasks. In this paper, an edge registration-based calibration algorithm is proposed for the online extrinsic calibration of RGB and ToF sensors. The proposed method automatically adjust the extrinsic parameters of the two sensors by an ICP-based edge registration algorithm. The cost function for the edge alignment process is carefully designed exploiting the geometric properties of the pixels on the edges. As a result, the edges extracted from the two heterogeneous sensors can be aligned with high accuracy. Experiments are executed in the simulated extraterrestrial environment to evaluate the accuracy and real-time performance of the calibration system. It is demonstrated that compared to the offline pattern board-based calibration, our method gets good performance on terms of both the accuracy and efficiency.

References

[1] M. Sutoh, Y. Sakakieda, M. Otsuki, and T. Kobayashi, "Surface sliding behavior analysis of space probes in simulated extraterrestrial environments," in 2021 IEEE/RSJ International Conference on Intelligent Robots and Systems (IROS), pp. 8774–8781, 2021.

[2] T. Hojnik, R. A. Dungavell, P. D. Flick, and J. M. Roberts, "Wheeled rovers with posable hubs for ter-

restrial and extraterrestrial exploration," IEEE Access, vol. 8, pp. 154318–154328, 2020.
[3] Y. Gao, T. E. Frame, and C. Pitcher, "Peircing the extraterrestrial surface: Integrated robotic drill for planetary exploration," IEEE Robotics & Automation Magazine, vol. 22, no. 1, pp. 45–53, 2015.
[4] K. Chitra, S. Dinesh, D. Mishra, V. Brinda, V. Lalithambika, and B. M. Kumar, "3D information retrieval for visual odometry system of planetary exploration rovers - a stereo vision approach," in 2013 International Conference on Advances in Computing, Communications and Informatics (ICACCI), pp. 354–360, 2013.
[5] S. Andolfo, F. Petricca, and A. Genova, "Visual odometry analysis of the NASA Mars 2020 perseverance rover's images," in 2022 IEEE 9th International Workshop on Metrology for AeroSpace (MetroAeroSpace), pp. 287–292, 2022.
[6] Y. Cheng, M. Maimone, and L. Matthies, "Visual odometry on the mars exploration rovers," in 2005 IEEE International Conference on Systems, Man and Cybernetics, vol. 1, pp. 903–910 Vol. 1, 2005.
[7] A. I. Mourikis, N. Trawny, S. I. Roumeliotis, A. E. Johnson, A. Ansar, and L. Matthies, "Vision-aided inertial navigation for spacecraft entry, descent, and landing," IEEE Transactions on Robotics, vol. 25, no. 2, pp. 264–280, 2009.
[8] K. Rice, J. Le Moigne, and P. Jain, "Analyzing range maps data for future space robotics applications," in 2nd IEEE International Conference on Space Mission Challenges for Information Technology (SMC-IT'06), pp. 1 pp.–, 2006.
[9] C. Park, J. J. Son, and S. Han, "Localization for mobile robots with a multi-ToF camera system," in 2022 22nd International Conference on Control, Automation and Systems (ICCAS), pp. 1771–1775, 2022.
[10] Y. Gao, J. Yuan, J. Jiang, Q. Sun, and X. Zhang, "Vido: A robust and consistent monocular visual-inertial-depth odometry," IEEE Transactions on Intelligent Transportation Systems, pp. 1–17, 2022.
[11] J. Kim, S. Park, S. Kim, and S. Lee, "Registration method between ToF and color cameras for face recognition," in 2011 6th IEEE Conference on Industrial Electronics and Applications, pp. 1977–1980, 2011.
[12] X. Li, W. Guo, M. Li, C. Chen, and L. Sun, "Generating colored point cloud under the calibration between TOF and RGB cameras," in 2013 IEEE International Conference on Information and Automation (ICIA), pp. 483–488, 2013.
[13] V. Gandhi, J. Čech, and R. Horaud, "High-resolution depth maps based on TOF-stereo fusion," in 2012 IEEE International Conference on Robotics and Automation, pp. 4742–4749, 2012.
[14] J. Zhu, L. Wang, R. Yang, and J. Davis, "Fusion of time-of-flight depth and stereo for high accuracy depth maps," in 2008 IEEE Conference on Computer Vision and Pattern Recognition, pp. 1–8, 2008.
[15] H. Gao, T. Wei, and S. Li, "High-precision extrinsic calibration method of a time-of-flight IMU RGB-camera with loop closure constraints," IEEE Sensors Journal, vol. 21, no. 21, pp. 24388–24397, 2021.
[16] J. Jung, J.-Y. Lee, Y. Jeong, and I. S. Kweon, "Time-of-flight sensor calibration for a color and depth camera pair," IEEE Transactions on Pattern Analysis and Machine Intelligence, vol. 37, no. 7, pp. 1501–1513, 2015.
[17] S. Huang, F. Gu, Z. Cheng, and Z. Song, "A joint calibration method for the 3D sensing system composed with ToF and stereo camera," in 2018 IEEE International Conference on Information and Automation (ICIA), pp. 905–910, 2018.
[18] L. Carrer, F. Zancanella, and L. Bruzzone, "Mars surface imaging by exploiting off-nadir radar sounding data," IEEE Transactions on Geoscience and Remote Sensing, vol. 59, no. 4, pp. 2951–2961, 2021.
[19] Q. Sun, J. Yuan, X. Zhang, and F. Duan, "Plane-Edge-SLAM: Seamless fusion of planes and edges for SLAM in indoor environments," IEEE Transactions on Automation Science and Engineering, vol. 18, no. 4, pp. 2061–2075, 2021.
[20] Z. Guo and Z. Xiao, "Research on online calibration of lidar and camera for intelligent connected vehicles based on depth-edge matching," Nonlinear Engineering, vol. 10, pp. 469–476, 12 2021.
[21] Y. Zhu, C. Li, and Y. Zhang, "Online camera-LiDAR calibration with sensor semantic information," in 2020 IEEE International Conference on Robotics and Automation (ICRA), pp. 4970–4976, 2020.
[22] J. Castorena, U. S. Kamilov, and P. T. Boufounos, "Autocalibration of lidar and optical cameras via edge alignment," in 2016 IEEE International Conference on Acoustics, Speech and Signal Processing (ICASSP), pp. 2862–2866, 2016.
[23] K. S. Arun, T. S. Huang, and S. D. Blostein, "Least-squares fitting of two 3-d point sets," IEEE Transactions on Pattern Analysis and Machine Intelligence, vol. 9, no. 5, pp. 698–700, 1987.
[24] J. Canny, "A computational approach to edge detection," IEEE Transactions on Pattern Analysis and Machine Intelligence, vol. PAMI-8, no. 6, pp. 679–698, 1986.